ACS APPLIED ENERGY MATERIALS

www.acsaem.org

Article

Phase Evolution of NaSICON Materials during Temperature-Dependent Conventional and Cold Sintering

Enkhtsetseg Dashjav, Monika Bhardwaj, Marie-Theres Gerhards, Qianli Ma, Katja Wätzig, Christoph Baumgärtner, Dörte Wagner, Ansgar Lowack, Mihails Kusnezoff, and Frank Tietz*

Cite This: *ACS Appl. Energy Mater.* 2025, 8, 11373−11381

Read Online

ACCESS | Metrics & More | Article Recommendations | Supporting Information

ABSTRACT: In this study, we investigated the impact of sintering temperature on the densification, phase formation, microstructure, crystallinity, and ionic conductivity of NaSICON materials with varying nominal Zr deficiency and a varying Si/P ratio. Several powder batches were synthesized and resulted in substantially different sintering abilities using conventional sintering. For most of the powder batches, the conventionally sintered specimens reached maximum ionic conductivities between 2 and 3 mS cm^{-1} after sintering at 1200−1300 °C. Cold sintering was explored using one of the powder batches with different sintering additives. After cold sintering, an annealing step at 900 °C yielded similar conductivities. Without postannealing, a maximum ionic conductivity of 0.55 mS cm^{-1} was reached at temperatures as low as 275 °C. There is clear evidence that (a) the densification temperature can be significantly reduced with increasing glass fraction in the specimens and (b) the total conductivity increases with increasing sintering temperatures due to increasing density and crystallinity.

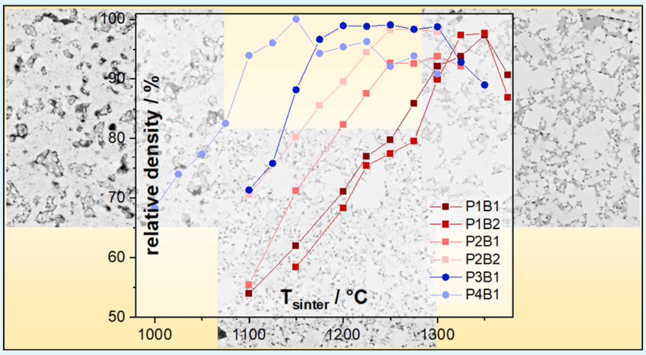

KEYWORDS: *cold sintering, conventional sintering, densification, phase formation, microstructure, ionic conductivity*

1. INTRODUCTION

Silicophosphates such as $Na_{1+x}Zr_2Si_xP_{3-x}O_{12}$ are promising materials for use as solid electrolytes in solid-state sodium batteries[1,2] or as protective layers to avoid adverse reactions between other battery materials.[3] Their appeal is based on their high ionic conductivity as well as the potentially low-cost starting materials combined with high compositional and structural flexibility.[1,4]

Among the compositions of the solid solution mentioned above, the compound with $x = 2$ has been investigated most due to its high ionic conductivity − 0.2 S cm^{-1} at 300 °C and 6.7×10^{-4} S cm^{-1} at 25 °C − which was reported in the very first publication on the properties of these materials,[5] therefore also called Na$^+$ superionic conductors (NaSICONs). However, there is increasing evidence that the compositions with $2.2 < x < 2.5$ have the highest conductivities[6−9] along this series. As an example, $Na_{3.4}Zr_2Si_{2.4}P_{0.6}O_{12}$ has an ionic conductivity of 5.2×10^{-3} S cm^{-1} at 25 °C.[8]

In addition to the above-mentioned solid solution, a compound emerged in the early 1980s, $Na_{3.1}Zr_{1.55}Si_{2.3}P_{0.7}O_{11}$, with high Zr deficiency and oxygen vacancies as well as high ionic conductivity (3×10^{-3} S cm^{-1} at 25 °C).[10] In subsequent publications, it became evident that $Na_{3.1}Zr_{1.55}Si_{2.3}P_{0.7}O_{11}$ consisted of two phases, and it was shown that a high amount of glass phase was present together with the crystalline NaSICON phase of a different stoichiometry than the nominal composition.[11−15] Very recently, it was shown that an increasing amount of glass fraction leads to a systematic decrease in the sintering temperature,[16] since the glass phase acts as a sintering aid.[11,15] Very similar decreases in the sintering temperatures were found when comparing the sintering properties of materials along the "Hong series" ($Na_{1+x}Zr_2Si_xP_{3-x}O_{12}$) and the "von Alpen series" ($Na_{1+y}Zr_{2-y/3}Si_yP_{3-y}O_{12-2y/3}$).[13]

In this work, we also compare materials from both series, but concentrate on the compositions $Na_{3.4}Zr_2Si_{2.4}P_{0.6}O_{12}$, $Na_{3.38}Zr_{1.69}Si_{2.51}P_{0.76}O_{12}$ (rewritten from $Na_{3.1}Zr_{1.55}Si_{2.3}P_{0.7}O_{11}$), $Na_{3.4}Zr_{1.85}Si_{2.45}P_{0.68}O_{12}$ − which is a composition between the two aforementioned stoichiometries[16] − and $Na_{3.4}Zr_{1.85}Si_{2.5}P_{0.63}O_{12}$ with a modified Si/P ratio. Additionally, different powder batches of the same composition are compared. The first three compositions are in line when the molar ratios of Zr, Si and P are displayed in a ternary

Received: May 20, 2025
Revised: July 1, 2025
Accepted: July 14, 2025
Published: July 29, 2025

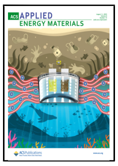

https://doi.org/10.1021/acsaem.5c01521
ACS Appl. Energy Mater. 2025, 8, 11373−11381

Table 1. Prepared Powder Batches, Their Specific Surface Area, and Characteristic Particle Size Parameters (d_{10}, d_{50}, and d_{90})

composition	abbreviated powder batch	BET surface[a]/$m^2\ g^{-1}$	d_{10}/μm	d_{50}/μm	d_{90}/μm
$Na_{3.4}Zr_2Si_{2.4}P_{0.6}O_{12}$	P1B1[b]	12.65	0.23	1.45 ± 0.12	6.43
$Na_{3.4}Zr_2Si_{2.4}P_{0.6}O_{12}$	P1B2	13.34	0.34	1.42 ± 0.05	4.98
$Na_{3.4}Zr_{1.85}Si_{2.5}P_{0.63}O_{12}$	P2B1	16.72	0.13	2.98 ± 0.20	6.24
$Na_{3.4}Zr_{1.85}Si_{2.5}P_{0.63}O_{12}$	P2B2	17.77	0.1	0.26 ± 0.01	3.00
$Na_{3.4}Zr_{1.85}Si_{2.45}P_{0.68}O_{12}$	P3B1	20.13	0.1	2.62 ± 0.09	6.58
$Na_{3.38}Zr_{1.69}Si_{2.51}P_{0.76}O_{12}$	P4B1	11.96	0.2	2.80 ± 0.13	6.32

[a] Experimental error: ± 10% [b] P1B1 = powder composition 1 − batch 1.

diagram (Figure S1 in the Supporting Information). Changing the Si/P ratio results in an arrangement in which the latter composition is perpendicular to the middle of the first three compounds. The possibility of reducing the sintering temperature with an increasing amount of glass additives[13,16−19] can also be solved with other sintering aids such as borates.[20,21] A further reduction in sintering temperature can be achieved by applying pressure and salt solutions, also known as "cold sintering process".

In recent years, Randall and co-workers published several papers on the cold sintering of different material classes at temperatures below 300 °C, in particular ferroelectric materials and ZnO.[22,23] In contrast to diffusion-dominated conventional sintering, the densification mechanism of cold sintering is based on dissolution and precipitation, meaning that an additive is required to support this effect, for example a Zn acetate solution for ZnO.[24] In addition to the process parameters (temperature, pressure, and time), the challenges posed by the densification kinetics during cold sintering are the investigation of appropriate additives (avoiding amorphous layers on the grain boundaries) and, later, the upscaling of the laboratory conditions to continuous processing.[25] In the case of NaSICON materials, the cold sintering of $Na_3Zr_2Si_2PO_{12}$ with 10 wt % NaOH solution resulted in a total ionic conductivity of up to 2.5×10^{-4} S cm^{-1} at 25 °C. For higher ionic conductivities, elevated cold sintering temperatures of up to 400 °C are required for a longer duration (3 h) or with postannealing.[26,27]

The cold sintering of Mg-substituted NaSICON at 140 °C and 780 MPa for 1 h with water as a transient liquid solution resulted in a poor ionic conductivity of 4.1×10^{-5} S cm^{-1}.[28] By annealing the cold-sintered electrolytes at 900 °C for 6 h, the conductivity could be increased to 6.1×10^{-4} S cm^{-1}. In addition to pure water, NaOH and KOH aqueous solutions were also tested as transient liquids for the cold sintering of Sc-substituted NaSICON at 250 °C and 300 MPa for 10 min.[27] Here, only low ionic conductivities of $\sim 1 \times 10^{-6}$ S cm^{-1} were achieved directly after cold sintering, which could be increased to $\sim 1 \times 10^{-5}$ S cm^{-1} for the NaOH additive and $\sim 4 \times 10^{-5}$ S cm^{-1} for the KOH additive by annealing for 1 h at 600 and 800 °C, respectively. A combination of cold sintering and liquid phase sintering of NaSICON with an aqueous Bi_2O_3 additive can achieve densities above 95% relative density and ionic conductivities of 9.1×10^{-4} S cm^{-1} by annealing cold-sintered electrolytes at 1000 °C for 6 h. This value is higher than those obtained with just the above-mentioned sintering methods.[29] All studies on cold sintering with aqueous transient liquids show that ionic conductivities $>1 \times 10^{-4}$ S cm^{-1} can only be achieved by subsequent thermal annealing at temperatures above 800 °C for several hours.

An outstanding high ionic conductivity of 2.4×10^{-4} S cm^{-1} for NaSICON solid electrolytes directly after cold sintering was achieved by using fused hydroxide additives to enhance the reactivity and solvent−particle interaction.[26] For this approach, NaSICON powder was mixed with dry NaOH flakes and then cold-sintered at 386 °C and 350 MPa for 3 h. At cold sintering temperatures of 350 to 400 °C, the molten NaOH (T_m = 312 °C) acts as a transient liquid phase.

Here, we report on a systematic investigation of the phase evolution and ionic conductivity of different NaSICON materials as well as a comparison of conventionally and cold-sintered ceramic pellets in order to gain a better understanding of the structure−property relationships. This work explores the impact of the sintering temperature on the densification, phase formation, microstructure, crystallinity, and ionic conductivity of the four compounds.

2. EXPERIMENTAL SECTION

The starting materials $NaNO_3$ (99.5%), $ZrO(NO_3)_2 \times H_2O$ (99%), and $Si(OC_2H_5)_4$ (99%) − supplied from VWR International (Belgium) − and $NH_4H_2PO_4$ (99.99%, Merck) were used as received. The Zr^{4+} precursor was prepared by dissolving the oxynitrate in deionized water. The amount of Zr was calculated on the basis of the ZrO_2 formed after the gravimetric analysis of the aqueous solution. The ZrO_2 content was about 0.1 g mL^{-1} based on the average of three samplings.

First, the nitrates were dissolved in deionized water using a quartz glass container. After dissolution, a stoichiometric amount of tetraethyl orthosilicate, $Si(OC_2H_5)_4$, was added, followed by a small amount of nitric acid to facilitate the dissolution. When the $Si(OC_2H_5)_4$ was hydrolyzed, a corresponding amount of $NH_4H_2PO_4$ was added and stirred for 30 min to form a homogeneous precipitation. The mixture was stirred overnight at 300 rpm and a temperature of 50 °C. The homogenized mixture was first heated up from 50 to 100 °C to slowly evaporate the water. Subsequently, the product was fired in a furnace at 800 °C for 3 h to form an amorphous raw powder. During this heat treatment, the inorganic polymer matrix was pyrolyzed, and NO_x, CO_2, and H_2O evolved as gaseous products. After this heat treatment, the primary particles of the powder display a nearly spherical shape with a diameter of <50 nm.[30] The calcined powders were then ball-milled in ethanol with zirconia balls on a roller bench at 200 rpm for 4 days. After drying, the powders were used either as prepared to this stage or conventionally sintered up to 1375 °C for 4 h. The quantity of each powder batch amounted to 800 g; characteristic powder properties of the calcined powders are listed in Table 1.

For cold sintering, the NaSiCON powder (P1B1) was crystallized at 1300 °C for 0.5 h. It was then mixed with 5 and 10 wt % borax (disodium tetraborate, $Na_2B_4O_7{\cdot}10H_2O$, >99.5%, Sigma-Aldrich) or 30 wt % of a 20 wt % $NaOH-NaNO_3$ (both >99%, Carl Roth) aqueous solution with a molar ratio of 81:19 using a pestle and mortar. The powder mixtures with borax additives were inserted into a stainless steel die with a diameter of 10 mm, and the filled die was placed in a high-pressure electro-hydraulic 2-column laboratory press (PW 40 EH-PRESSYS, P/O/Weber GmbH, Remshalden, Germany) with a heating−cooling plate system (HKP 500, P/O/Weber GmbH). To ensure a uniform temperature distribution during sintering, the pellet die was covered by a heating band. Applying a pressure of 600

MPa, cold sintering was performed at 140 and 200 °C. The cold sintering of NaSICON with NaOH−$NaNO_3$ aqueous solution was performed in a tungsten carbide pressing die with an inner diameter of 17 mm, since tungsten carbide is more stable against hydroxide additives.[31] A nickel foil was used to separate the ceramic powder from the tungsten carbide punches. Cold sintering was then performed at a pressure of 600 MPa and a temperature of 275 °C for 2 h. In this case, the die was heated exclusively by the heating plates of the hot press without using the heating sleeves.

The particle size distribution was measured by a laser scattering particle analyzer (Horiba LA-950 V2) using a suspension prepared by ultrasonication of the NaSICON powders in ethanol. The elemental composition of the calcined powders was controlled by inductively coupled plasma optical emission spectroscopy (ICP-OES). The sintering behavior was initially determined by dilatometry measurements (DIL 402C, Netzsch) using cylindrical pellets with a diameter of 8 mm. For conventional sintering experiments in a chamber furnace, the calcined powders were uniaxially pressed using a pressing mold with a diameter of 13 mm and by applying a pressure of 135 MPa. They were then heat-treated in a temperature range of 1000 to 1375 °C with a dwell time of 4 h and a ramp rate of 5 K min^{-1}. The density of the NaSICON ceramics was measured according to the weight and volume of the sintered pellets. To determine the relative density of the ceramics, values of 3.28, 3.23, and 3.15 g cm^{-1} were used for P1, P2 & P3, and P4, respectively, taking into account the volume fraction of the glass $Na_2Si_2O_5$[16] and its density (2.4 g cm^{-1}). The range of absolute error of the relative density of each sample is 1−3%.

The crystallographic phase analyses were carried out using the Bruker D4 X-ray diffractometer with scanning parameters of 0.02° as step size and 1.5 s/step. The HighScore software suite[32] was used for qualitative phase analysis of the X-ray diffraction (XRD) patterns of the polycrystalline powders and the sintered pellets. The crystallographic software package Powder cell was used for preliminary quantification of the phases.[33] The calculated residual profile parameter (R_p) and residual for Bragg positions (R_{Bragg}) were about 10% and <7%, respectively. The estimated deviation in lattice parameters vary between ±0.001 and 0.0005 Å and the error in phase quantification is ±1−5 wt % since the secondary phases are well-separated. The XRD patterns, refined lattice parameters, and phase fractions are given in the Supporting Information (Figures S1, S2 and Table S1). The sintered pellets were embedded in EpoFix Resin (Struers Inc.) and polished with sandpaper using water-free cutting fluid (Struers Inc.). The samples were fine-polished using water-free diamond suspensions with grain sizes of 9, 3, and 1 μm (Cloeren Technology GmbH). After the metallographic preparations, the microstructure of the specimens was analyzed by scanning electron microscopy (GeminiSEM 450 ZEISS; Carl Zeiss Microscopy GmbH, Oberkochen, Germany) after being coated with a thin Pt layer to avoid charging effects. For ionic conductivity measurements, the sintered NaSICON pellets were sputtered with Au on both sides. The cold-sintered samples were transferred to a heatable airlock connected to an argon-filled glovebox where they were heated at 140 °C for 24 h to remove any remaining moisture. Subsequently, the heat-treated samples were sealed in argon atmosphere in gastight test cells (EL-Cell GmbH). The impedance spectra were recorded by a commercial electrochemical system (VMP-300; Bio-Logic SAS) in the AC frequency range from 7 MHz to 1 Hz at 25 °C. An alternating voltage amplitude of 20 mV was used during measurements. The impedance data were fitted using the ZView software (Scribner Associates Inc.).

3. RESULTS AND DISCUSSION

3.1. Characterization of Calcined Powders. The chemical analysis with ICP-OES of the calcined NaSICON powders revealed good agreement between the determined atomic ratios of the constituent elements and the nominal composition (see Tables 1 and 2). Only a few atomic ratios show a higher deviation from the expected atomic ratios, such as the Na content in P2B1 (+5.4%), which might have a significant impact on the sintering and physical properties,[34,35] the Zr (−4.3%) and P (+8.4%) content in P3B1, and, finally, the Si content (+4.4%) in P4B1. The latter deviations may have an influence on the glass formation, meaning that different microstructures may be expected to those reported on previously.[16]

Table 2. Results of the ICP-OES Analysis of the NaSICON Powders after Calcination at 800 °C, Normalized to 12 mol Oxygen per Formula Unit[a]

powder	Na	Zr	Si	P
P1B1	3.430	1.958	2.454	0.584
P1B2	3.341	1.981	2.439	0.596
P2B1	3.584	1.841	2.491	0.617
P2B2	3.416	1.852	2.507	0.629
P3B1	3.467	1.771	2.435	0.737
P4B1	3.262	1.638	2.632	0.731

[a] Experimental errors for the elements are ± 3 wt %. In atomic ratios, this means ΔNa = ± (0.087−0.089), ΔZr = ± (0.033−0.041), ΔSi = ± (0.041−0.044), and ΔP = ±(0.016 − 0.017).

The XRD patterns of the calcined powders showed broad reflections indicating large disorder and/or very small grain sizes (Figure 1). The full range of the measured XRD patterns from 10° to 80° is available as Figure S2 in the Supporting Information. The XRD patterns are dominated by the reflections of the NaSICON phase and the parakeldyshite-type $Na_2ZrSi_2O_7$ as indicated by the red and black short vertical lines, respectively, of the reference patterns at the bottom of Figure 1. The reflections related to $Na_2ZrSi_2O_7$ are additionally marked by the three transparent gray areas. The presence of ZrO_2 and Na_2ZrSiO_5, which were also to be expected, cannot be clearly confirmed in all cases.

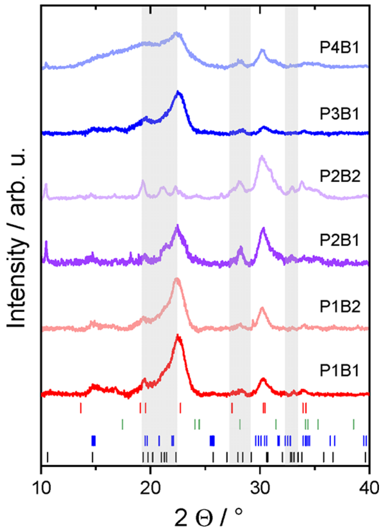

Figure 1. XRD patterns of the powders calcined at 800 °C. For comparison, from top to bottom, the position of the reflections of rhombohedral NaSICON, monoclinic ZrO_2, Na_2ZrSiO_5, and $Na_2ZrSi_2O_7$ are marked as short vertical lines at the bottom of the image. The three transparent gray areas highlight the groups of reflection of $Na_2ZrSi_2O_7$.

The powders can thus be classified into three groups: (a) P1B1 and P1B2 show a good match of the NaSICON reflections and negligible contribution of $Na_2ZrSi_2O_7$, (b)

P2B1 and P2B2 reveal NaSICON as well as $Na_2ZrSi_2O_7$ reflections. The presence of $Na_2ZrSi_2O_7$ is not only confirmed by the reflection intensities in the three transparent gray areas, but also by the peak appearing at $2\Theta = 10.48°$. However, there is a substantial difference of intensities of the NaSICON reflections between P2B1 and P2B2. (c) P3B1 and especially P4B1 are the powders with the highest amorphous amounts in the 2Θ-region of 15−20°. They also have the highest Zr deficiency and tend to form larger amounts of glass phase. Although the pattern of P4B1 shows contributions of NaSICON as well as $Na_2ZrSi_2O_7$, it is the most unresolved with very broad reflections.

3.2. Sintering Properties. The sintering behavior of the as-calcined powders was first examined by dilatometry, where the dimensional change of a pellet is measured in relation to the increase in temperature (Figure S3 in the Supporting Information). For the dilatometry measurements, the same heating rate was used as for the sintering experiments in the chamber furnace. The pellets hardly shrink up to a temperature of 800 °C, maintaining about 95% of their original thickness. This is followed by a first shrinkage step between 800 and 950 °C, at which temperature residues of Na_2CO_3 in the powders melt, start to release carbon dioxide, and become the reactive agent for the initial sintering as well as the subsequent crystallization period. This intermediate crystallization, typically at a temperature of up to 1200 °C, is characterized by low shrinkage rates, as the formation of a crystalline lattice generates an increase in volume and counteracts the sintering process. Beyond 1200 °C, the second shrinkage step again shows high shrinkage rates, indicating the active densification behavior of the NaSICON powders.

The uniaxially pressed cylindrical pellets were sintered in a chamber furnace at temperatures ranging from 1000 to 1375 °C in steps of 25 °C to investigate densification and phase formation during the sintering process.

The relative density of the NASICON ceramics increased in an almost linear fashion with the sintering temperature until densities of about 95−97% were reached (Figure 2). Beyond this characteristic temperature, the densities initially remained constant for a certain temperature interval before subsequently declining again. The regime of constant densities strongly depended on the Zr deficiency, affecting both the width and the beginning of this temperature range. Whereas the nearly stoichiometric powders P1B1 and P1B2 showed pronounced retarded sintering and only a narrow temperature range with densities of more than 95%, the temperature at constant density decreased along the powders P2, P3, and P4 with decreasing Zr content. This is in good agreement with previous observations.[16] Similarly, the decrease in density at high temperatures shifted to lower temperatures. Since the decreasing densities were clearly related to the pore formation of evaporating Na_2O from the glass phase,[16] the changing glass composition seems to accelerate this process.

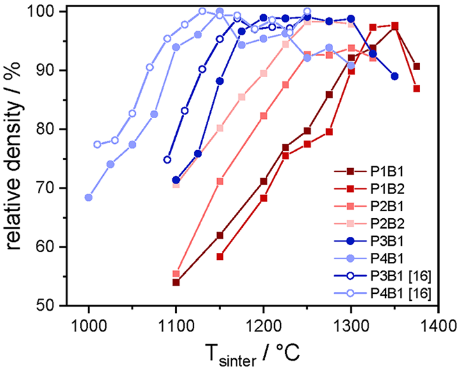

Figure 2. Densification of the NaSICON powders as a function of the sintering temperature. Open circles depict the data taken from ref 16.

The densification of NaSICON is influenced significantly by cold sintering at a high pressure of 600 MPa and additives used to improve the solution and precipitation mechanism. The addition of 10 wt % borax as a sintering aid resulted in bulk densities of 93.8 and 94.4% at $T = 140$ °C and $T = 200$ °C, respectively. Samples with 5 wt % borax additive only achieved smaller relative densities of 87.0 and 87.6% at 140 and 200 °C, respectively. With both additive concentrations, samples cold-sintered at 200 °C are prone to cracking during demolding.

For NaOH−$NaNO_3$ additives, a geometrical density of 85.8% was achieved after cold sintering at 275 °C. A density of 95% was previously reported by Grady et al.[26] for a hydroxide additive and cold sintering at $T = 400$ °C. Compared with conventionally sintered samples of powder P1B1, the sintering temperature is reduced by nearly 1000 °C to achieve comparable relative densities using the cold sintering process.

3.3. Phase Formation. XRD was used to determine the phase evolution and the dependence of lattice parameters on the applied sintering temperatures. During the subsequent sintering steps, the NaSICON phase had already formed as the majority phase at 1100 °C (Figure 3). In addition, small amounts of secondary phases such as ZrO_2 and $Na_2ZrSi_2O_7$ were present, which gradually vanished with increasing sintering temperature (see also Figure S4). It is interesting to note that between 1000 and 1200 °C the amount of $Na_2ZrSi_2O_7$ increased with the analytical Zr deficiency. At 1250 °C, all powders showed NaSICON with a phase purity of >99.5% wt %. At even higher temperatures, $Na_2ZrSi_2O_7$ appeared again as a decomposition product, amounting up to 10% at 1325 °C.

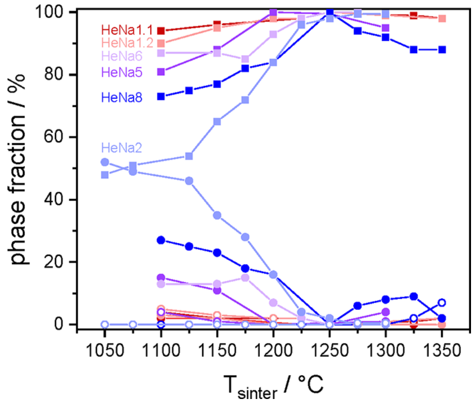

Figure 3. Phase evolution of the NaSICON powders as a function of the sintering temperature. Filled squares, filled circles, and open circles represent the phase fraction of NaSICON, $Na_2ZrSi_2O_7$, and ZrO_2, respectively.

The existence of rhombohedral and monoclinic NaSICON modification, or their separation, can still not be systematically explained using XRD, specifically the ordering of fractional occupancies of the Na ions and the disorder of Si/P sites. Previous neutron diffraction analyses on the series $Na_{3.4}Zr_{2-3a/4}Si_{2.4+a/4}P_{0.6+1.5a/4}O_{12-a/16}$ $(0 < a < 0.8)$[16] with

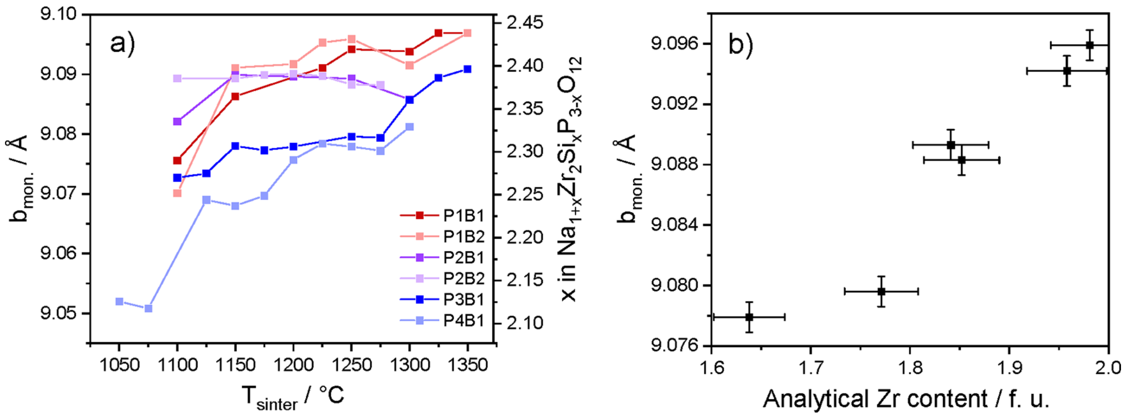

Figure 4. (a) Dependence of lattice parameter *b* for the monoclinic NaSICON phase on sintering temperature. The right *y*-axis gives a tentative sodium content in the formed NaSICON phase. (b) Dependence of lattice parameter *b* on the analytical Zr content after sintering of the samples at 1250 °C.

increasing Zr deficiency resulted in assigning the diffraction patterns to the monoclinic phase in the whole series. For the phase evolution analyses versus sintering temperature, the obtained patterns were therefore indexed as monoclinic, although some samples also contained fractions of the rhombohedral modification.

The lattice parameter *b* in the monoclinic modification increases with increasing sintering temperature, primarily indicating the formation of NaSICON from the secondary phases as well as the distribution of ions for structural relaxation processes, which is likely triggered by the Zr content (see below). Since the lattice parameter increases nearly linearly with the sodium content,[11,16] the right *y*-axis in Figure 4a can be used to read the sodium stoichiometry of the NaSICON phase at different stages of structural evolution. For most of the samples, except P2B1 and P2B2, the lattice parameter increased gradually with increasing sintering temperature, whereas it remained almost constant for the two samples mentioned above. Since all NaSICON samples are (nearly) phase-pure at 1250 °C (Figures 3, S5 and Table S1), the lattice parameter at this temperature tentatively reflects the sodium content of the formed NaSICON phase. A further increase of the lattice parameter can be regarded as the beginning of a phase decomposition. The lattice parameter *b* of the samples sintered at 1250 °C also shows a strong correlation with the Zr content in the materials (Figure 4b), which indicates that the sodium content is not only determined by the Si/P ratio but also essentially by the Zr content.

To verify a correlation between phase evolution and crystallographic properties, such as the crystallinity and compositional homogeneity of the NaSICON solid electrolytes, the crystallinity was estimated from the shape of the XRD reflections expressed by the full width at half-maximum (FWHM) of the diffraction peaks. Here, the strong single peak (200) at $2\Theta = 13.6°$ was selected for FWHM analysis due to the overlap of other NaSICON peaks with the reflections of the secondary phases (see Figures S4 and S5). For the profile fitting, a pseudo-Voigt function was used with half Gaussian and half Lorentzian contributions. Figure S6a shows the correlation between the FWHM of the (200) peak and sintering temperature. The FWHM is inversely proportional to the crystallinity which is shown in Figure S6b. To calculate the average crystallite size, the Debye–Scherrer equation was used with the Scherrer constant $K = 0.9$ and the X-ray wavelength $\lambda = 0.15418$ nm. The crystallite sizes become larger with increasing sintering temperature (Figure S6b). It must be stressed here that the crystallite size is not equal to the particle size as shown in the next chapter, but should be understood as a crystal fraction with uniform XRD scattering.

At 800 °C, the (200) peak could not be clearly observed and was hidden under the broad hump-like profile between 12° and 18° (see Figure 1). The crystallinity drastically increased above 1000 °C and then slowly saturated around 1275 °C with a FWHM value of 0.12° and a crystallite size of 70 nm for P2B2 as an example (Figure S4a,b). This tendency is also observed for the other powder batches.

To investigate the possible degradation of the NaSICON material during cold sintering, the phase composition of the cold-sintered samples was examined. The XRD patterns are shown in Figure 5. All cold-sintered samples mainly show reflections of the NaSICON phase, independent of the additive used. Compared with the pristine powder, no additional reflections caused by decomposition can be observed. Secondary phases originating from the sintering additives are not visible in the XRD patterns of the borax additive samples. Only for samples cold-sintered with the NaOH–$NaNO_3$

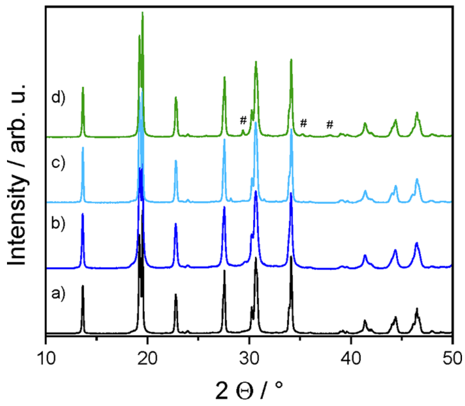

Figure 5. XRD patterns of cold-sintered and postannealed samples: (a) pristine powder, (b) cold-sintered at 140 °C with 10 wt % borax additive, (c) cold-sintered at 140 °C with 10 wt % borax additive and subsequent postannealing at 900 °C, and (d) cold-sintered at 275 °C with 30 wt % NaOH–$NaNO_3$ additive (# indicates $NaNO_3$).

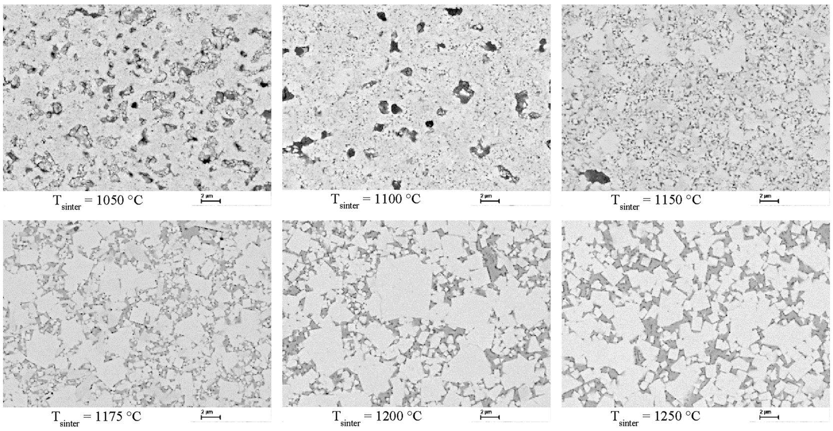

Figure 6. SEM images of polished cross sections showing the microstructural evolution of sintered pellets of P4B1. White and compact particles correspond to NaSICON; gray areas show the glass fraction; and small black dots are nm-sized pores.

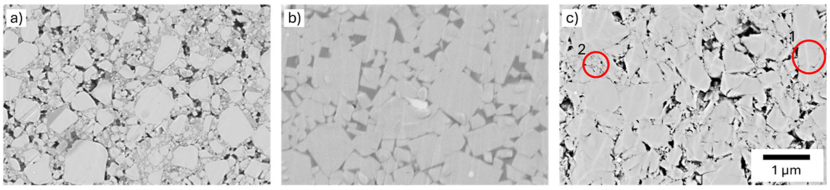

Figure 7. SEM images of polished cross sections showing the microstructure of cold-sintered NaSICON electrolytes: (a) cold-sintered at 140 °C with 10 wt % borax additive; (b) cold-sintered at 140 °C with 10 wt % borax additive and subsequent postannealing at 900 °C; and (c) cold-sintered at 275 °C with 30 wt % NaOH−$NaNO_3$ additive. In panel (c), the red circles indicate (1) the areas with intimate grain-to-grain contact and (2) the sintering of very fine particles.

additive can small reflections of $NaNO_3$ be seen in the XRD patterns (denoted by # symbol).

3.4. Microstructure.

For the conventionally sintered samples, the evolution of the microstructure with increasing sintering temperature is best visualized with the samples of powder P4B1, which has the highest Zr deficiency. Here, not only the reduction in porosity and the grain growth can be observed as in stoichiometric and more crystalline NaSICON materials,[36] but also the phase formation and segregation of the crystalline and glass phase. The difference in the microstructure of samples sintered at 1050 and 1100 °C is mainly characterized by the reduction of porosity (see Figure 6), the particles have a subμm size. A remarkable microstructural change occurs at 1150 °C. At this temperature, most of the larger pores disappear, the first angular crystals are formed, and a large number of triple points are filled with material, which can be seen as the beginning of the formation of the glass phase. After sintering at 1175 °C, the crystallization of NaSICON particles is much more pronounced and the glass is clearly visible around the crystals as the phase with the darker gray scale. In addition, nm-sized porosity is visible as small black dots at NaSICON/glass interfaces. At the highest sintering temperatures, 1200 and 1250 °C, the microstructure is consolidated with larger NaSICON particles, a more segregated glass phase, and more nm-sized pores. At 1250 °C, the NaSICON crystals seem to have a more uniform and rectangular shape.

The microstructure of NaSICON cold-sintered at 140 °C with 10 wt % borax additive is shown in Figure 7a. Beside the NaSICON particles, pores and a secondary phase from residual borax can be seen. Since no other phases, except the NaSICON phase, are visible in the XRD pattern, this phase is amorphous and encapsulates the NaSICON particles. After postannealing at 900 °C, significant differences in the microstructure can be observed (Figure 7b). The fine NaSICON particles disappeared and a structure of interconnected, large NaSICON particles formed. At 900 °C, the borax additive forms a liquid phase, which increases the sintering of particles and particle growth. The mechanistic similarity of sintering with liquid phase and cold sintering has been reported elsewhere.[25] After postannealing, the secondary phase is still present in the microstructure (dark gray regions). However, in contrast to only cold-sintered samples, the secondary phase no longer encapsulates the NaSICON particles. Additional ZrO_2 particles (white grains) are visible. After cold sintering with NaOH−$NaNO_3$ additive at 275 °C, the microstructure of NaSICON also forms good contacts between large NaSICON particles (see Figure 7c, area 1) without forming a secondary phase between the particles, i.e., no significant amount of NaOH−$NaNO_3$ remains in the porosity of the sample. Compared with the result using borax additive, clear indications of sintering are visible in the regions with very fine particles (see area 2). This observation points to decomposition of the NaOH−$NaNO_3$ additive and dissolution of Na_2O in the NaSICON particles as it has been similarly reported for cold sintering of lithium ion-conductors in combination with the underlying mechanistic processes.[37]

3.5. Ionic Conductivity.

The total ionic conductivity of the NASICON specimens sintered between 1000 and 1350 °C was investigated by impedance spectroscopy (Figure 8). The impedance spectra of all samples displayed only one semicircle or "time constant" and were fitted using a pure resistance, R_0, and two parallel $R-C$ (resistor−capacitor) equivalent circuit elements in series. However, instead of an ideal capacitor, a constant phase element (CPE) or "imperfect" capacitor was employed to represent the capacitive contribution. The

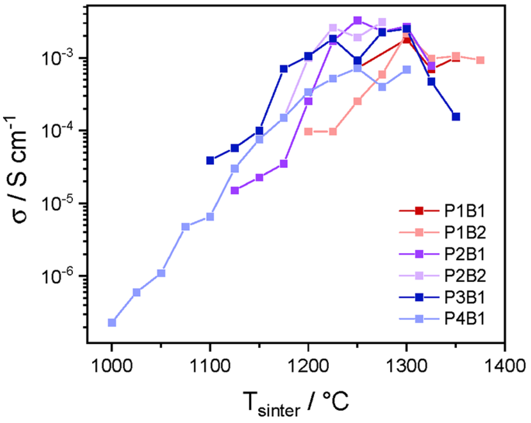

Figure 8. Total ionic conductivity measured at 25 °C after sintering the pellets at various temperatures. The impedance values were normalized to the size of the pellets. The error during fitting of the impedance spectra varied between 2% for well resolved semicircles up to 12% for semicircles overlapping with the electrode response (see Figure S7), which corresponds to the symbol size in this figure and Figure 9.

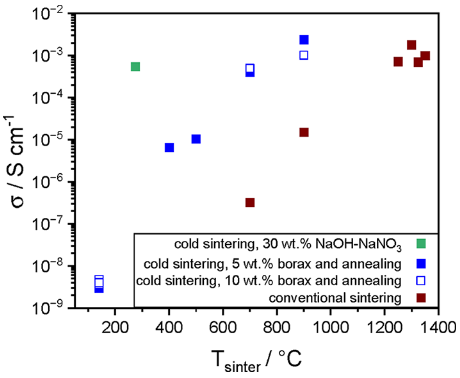

Figure 9. Total ionic conductivity measured at 25 °C after cold sintering of the powder mixtures with the NaOH−NaNO$_3$ additive (green symbol) and borax, additionally with postannealing at various temperatures between 400 and 900 °C (filled blue and open blue symbols for 5 and 10 wt % borax, respectively), compared with conventionally sintered powder compacts of P1B1 (dark red symbols).

imperfectness is expressed as an exponent, *n*, of the *R-CPE* circuit, which is an additional parameter for data fitting. The capacitance values calculated using the fitting parameters were in the range of 10^{-10}−10^{-8} F. The obtained semicircles can therefore be unambiguously assigned to the grain boundary resistance, R_{gb}.[38] The second *R-CPE* circuit is associated with the electrode contribution. Impedance spectra of samples measured at 1150, 1200, and 1250 °C are displayed as Figure S7a−c, respectively, in the Supporting Information.

The total conductivity of the samples was derived from the resistance values (R_0 + R_{gb}) and plotted against the sintering temperatures in Figure 8. The total ionic conductivity exponentially increases with increasing density and crystallinity, and reaches up to 2−3 mS cm^{-1} at 1200−1300 °C. This value is slightly lower than the previously reported values for $Na_{3.4}Zr_2Si_{2.4}P_{0.6}O_{12}$,[8] but is still in very good agreement with a recent study.[39] Only the samples of P4B1 do not exceed the value of 0.7 mS cm^{-1}. Above a sintering temperature of 1300 °C, the conductivity typically decreases again due to the decrease in density (Figure 2) caused by the evaporation of Na_2O and the partial decomposition of the NaSICON (Figure 3).

The cold sintering of NaSICON at T = 140 °C increased the density to 87.0 and 93.8% using 5 and 10 wt % borax additive, respectively, but the total ionic conductivity with ∼10^{-9} S cm^{-1} was very low and independent of the additive concentration (Figure 9). Although the cold-sintered samples at 200 °C have a slightly higher density, they are prone to cracking during demolding, as mentioned above. The thermal annealing experiments of borax-added NaSICON were therefore only performed with samples cold-sintered at 140 °C. As the postannealing temperature rises, the ionic conductivity increases from 6.5 × 10^{-6} S cm^{-1} at T = 400 °C to 2.4 × 10^{-3} S cm^{-1} at T = 900 °C for 5 wt % additive concentration. The latter value is in the same range of ionic conductivity as that measured on conventionally sintered NaSICONs, whereas the required temperature is about 400 K lower. This temperature reduction is a significant advance in the processing of NaSICON materials. In comparison to this result, the directly cold-sintered NaSICON with NaOH−NaNO$_3$ additive at T = 275 °C achieved a total ionic conductivity of 5.5 × 10^{-4} S cm^{-1} with 85.8% density (Figure 9). During the preparation of the cell, any residual water was eliminated by heat treatment at 140 °C, as outlined in the experimental section. Additionally, the SEM image (Figure 7c) shows no evidence of remaining secondary phases, leading to the conclusion that proton conductivity does not significantly influence the overall ionic conduction. In comparison to Grady et al.,[26] the temperature was reduced for the cold sintering from 386 to 275 °C, with a slight increase of the total ionic conductivity using a low-melting eutectic salt mixture instead of pure NaOH.

4. CONCLUSIONS

The temperature-dependent investigation of the phase evolution of four different NaSICON compositions revealed substantial differences among the synthesized powder batches, but can be primarily attributed to the Zr deficiency of the prepared NaSICONs. The increasing degree of Zr deficiency revealed the following observations:

1. the densification of the NaSICON powders shifts toward lower sintering temperatures due to the increasing amount of glass phase
2. there is a consistent increase of $Na_2ZrSi_2O_7$ formation at sintering temperatures below 1200 °C, whereas at 1250 °C, all compositions are pure NaSICON materials
3. the monoclinic lattice parameter, *b*, which is strongly correlated with the sodium content, decreases in an almost linear fashion
4. the ionic conductivity is significantly dependent on the sintering temperature, but reaches 2−3 mS cm^{-1} − except for the powder with the highest Zr deficiency (0.7 mS cm^{-1}).

The cold sintering of the NaSICON powder with the composition $Na_{3.4}Zr_2Si_{2.4}P_{0.6}O_{12}$ resulted in relative densities of 90 ± 5% using borax or NaOH−NaNO$_3$ as a sintering additive. With the borax additive, postannealing at 900 °C is necessary to obtain a similar ionic conductivity to that of conventionally sintered samples—a heat treatment that is 300−400 °C lower than usual sintering temperatures. In contrast, cold sintering with NaOH−NaNO$_3$ directly resulted in 5.5 × 10^{-4} S cm^{-1}, with great potential for further improvements.

ASSOCIATED CONTENT

Supporting Information

The Supporting Information is available free of charge at https://pubs.acs.org/doi/10.1021/acsaem.5c01521.

> Powder XRD patterns after calcination at 800 °C; powder XRD patterns of batch P2B1; powder XRD patterns of the NaSICON powders after sintering at 1250 °C; lattice parameters and phase fractions of NaSICON powders depending on sintering temperature, dilatometric sintering curves, dependence of peak shape, and crystallite size on sintering temperature; and impedance spectra recorded at different temperatures (PDF)

AUTHOR INFORMATION

Corresponding Author

Frank Tietz − *Institute of Energy Materials and Devices, IMD-2: Materials Synthesis and Processing, Forschungszentrum Jülich GmbH, D-52425 Jülich, Germany; Institute of Energy Materials and Devices, IMD-4: Helmholtz Institute Münster−Ionics in Energy Storage, Forschungszentrum Jülich GmbH, D-52425 Jülich, Germany;* orcid.org/0000-0002-3724-7627; Phone: +49-2461-615007; Email: f.tietz@fz-juelich.de

Authors

Enkhtsetseg Dashjav − *Institute of Energy Materials and Devices, IMD-2: Materials Synthesis and Processing, Forschungszentrum Jülich GmbH, D-52425 Jülich, Germany;* Present Address: German Aerospace Center (DLR), Institute of Future Fuels, Solar Chemical Process Development, Linder Höhe, D-51147 Cologne, Germany; orcid.org/0000-0002-7823-7759

Monika Bhardwaj − *Institute of Energy Materials and Devices, IMD-2: Materials Synthesis and Processing, Forschungszentrum Jülich GmbH, D-52425 Jülich, Germany*

Marie-Theres Gerhards − *Institute of Energy Materials and Devices, IMD-2: Materials Synthesis and Processing, Forschungszentrum Jülich GmbH, D-52425 Jülich, Germany*

Qianli Ma − *Institute of Energy Materials and Devices, IMD-2: Materials Synthesis and Processing, Forschungszentrum Jülich GmbH, D-52425 Jülich, Germany;* orcid.org/0000-0002-4709-4927

Katja Wätzig − *Fraunhofer Institute for Ceramic Technologies and Systems IKTS, D-01277 Dresden, Germany;* orcid.org/0000-0003-2606-8065

Christoph Baumgärtner − *Fraunhofer Institute for Ceramic Technologies and Systems IKTS, D-01277 Dresden, Germany;* orcid.org/0000-0002-8102-1262

Dörte Wagner − *Fraunhofer Institute for Ceramic Technologies and Systems IKTS, D-01277 Dresden, Germany*

Ansgar Lowack − *Fraunhofer Institute for Ceramic Technologies and Systems IKTS, D-01277 Dresden, Germany*

Mihails Kusnezoff − *Fraunhofer Institute for Ceramic Technologies and Systems IKTS, D-01277 Dresden, Germany*

Complete contact information is available at: https://pubs.acs.org/10.1021/acsaem.5c01521

Author Contributions

E.D.: Data curation, formal analysis, investigation, validation, writing (review and editing); M.B.: Data curation, investigation; M.-T.G.: Resources, investigation; Q.M.: Data curation, formal analysis, investigation, writing (review and editing); K.W.: Data curation, formal analysis, investigation, writing (review and editing); C.B.: Formal analysis, investigation, validation, writing (review and editing); D.W.: Formal analysis, investigation, writing (review and editing); A.L.: Data curation, formal analysis, investigation, writing (review and editing); M.K.: Conceptualization, funding acquisition, formal analysis, funding acquisition, project administration, supervision, visualization, writing (review and editing); F.T.: Conceptualization, methodology, data curation, formal analysis, funding acquisition, supervision, visualization, writing (original draft), writing (review and editing).

Notes

The authors declare no competing financial interest.

ACKNOWLEDGMENTS

We thank Dr. D. Sebold (FZJ, IMD-2) for the SEM investigations, V. Bader (FZJ, IMD-2) for technical assistance, and colleagues at ZEA-3 (FZJ) for the ICP-OES measurements. We are also grateful for the financial support provided by the German Federal Ministry of German Federal Ministry of Education and Research (BMBF) as part of the "HeNa" project (support codes: 13XP0390A and 13XP0390B). The authors take responsibility for the content of this publication. Furthermore, we acknowledge support by the Open Access Publication Agreement between ACS and Research Center Jülich.

REFERENCES

(1) Ma, Q.; Tietz, F. Solid-state electrolyte materials for sodium batteries: Towards practical applications. *ChemElectroChem.* **2020**, *7*, 2693−2713.

(2) Lan, T.; Tsai, C.-L.; Tietz, F.; Wei, X.-K.; Heggen, M.; Dunin-Borkowski, R.; Wang, R.; Xiao, Y.; Ma, Q.; Guillon, O. Room-temperature all-solid-state sodium batteries with robust ceramic interface between rigid electrolyte and electrode materials. *Nano Energy* **2019**, *65*, No. 104040.

(3) Goodwin, L. E.; Till, P.; Bhardwaj, M.; Nazer, N.; Adelhelm, Ph.; Tietz, F.; Zeier, W. G.; Richter, F. H.; Janek, J. Protective NaSICON Interlayer Between a Sodium Tin Alloy Anode and Sulfide-based Solid Electrolytes for All-Solid-State Sodium Batteries. *ACS Appl. Mater. Interfaces* **2023**, *15*, 50457−50468.

(4) Guin, M.; Tietz, F. Survey of the transport properties of NASICON materials for use in sodium batteries. *J. Power Sources* **2015**, *273*, 1056−1064.

(5) Goodenough, J. B.; Hong, H.-Y. P.; Kafalas, J. Fast Na^+-ion transport in skeleton structures. *Mater. Res. Bull.* **1976**, *11*, 203−220.

(6) Kafalas, J. A.; Cava, R. J. Effect of pressure and composition on fast Na^+-ion transport in the system $Na_{1+x}Zr_2Si_xP_{3-x}O_{12}$. In *Fast ion transport in solids - Proc. Int. Conf. Fast Ion Transport in Solids, Electrodes, and Electrolytes*; Vashishta, P.; Mundy, J. N.; Shenoy, G. K., Eds.; Elsevier North Holland: 1979; pp 419−422.

(7) Vogel, E. M.; Cava, R. J.; Rietman, E. Na^+ ion conductivity and crystallographic cell characterization in the Hf-NASICON system $Na_{1+x}Hf_2Si_xP_{3-x}O_{12}$. *Solid State Ionics* **1984**, *14*, 1−6.

(8) Ma, Q.; Tsai, C.-L.; Wei, X.-K.; Heggen, M.; Tietz, F.; Irvine, J. T. S. Room temperature demonstration of a sodium superionic conductor with grain conductivity in excess of 0.01 S cm^{-1} and its primary applications in symmetric battery cells. *J. Mater. Chem. A* **2019**, *7*, 7766−7776.

(9) Deng, Z.; Mishra, T. P.; Mahayoni, E.; Ma, Q.; Tieu, A. J. K.; Guillon, O.; Chotard, J.-N.; Seznec, V.; Cheetham, A. K.; Masquelier, C.; Gautam, G. S.; Canepa, P. Fundamental investigations on the sodium-ion transport properties of mixed polyanion solid-state battery electrolytes. *Nat. Commun.* **2022**, *13*, 4470.

(10) von Alpen, U.; Bell, M. F.; Höfer, H. Compositional dependence of the electrochemical and structural parameters in the Nasicon system ($Na_{1+x}Si_xZr2P_{3-x}O_{12}$). *Solid State Ionics* **1981**, *3–4*, 215–218.

(11) Engell, J.; Mortensen, S.; Møller, L. Fabrication of Nasicon electrolytes from metal alkoxide derived gels. *Solid State Ionics* **1983**, *9–10*, 877–884.

(12) Yde-Andersen, S.; Lundgaard, J. S.; Møller, L.; Engell, J. Properties of nasicon electrolytes prepared from alkoxide derived gels: Ionic conductivity, durability in molten sodium and strength test data. *Solid State Ionics* **1984**, *14*, 73–79.

(13) Kuriakose, A. K.; Wheat, T. A.; Ahmad, A.; Dirocco, J. Synthesis, Sintering, and Microstructure of Nasicons. *J. Am. Ceram. Soc.* **1984**, *67*, 179–183.

(14) Perthuis, H.; Colomban, Ph. Sol-gel routes leading to nasicon ceramics. *Ceram. Int.* **1986**, *12*, 39–52.

(15) Go, W.; Kim, J.; Pyo, J.; Wolfenstine, J. B.; Kim, Y. Investigation on the Structure and Properties of $Na_{3.1}Zr_{1.55}Si_{2.3}P_{0.7}O_{11}$ as a Solid Electrolyte and Its Application in a Seawater Battery. *ACS Appl. Mater. Interfaces* **2021**, *13*, 52727–52735.

(16) Dashjav, E.; Gerhards, M.-T.; Klein, F.; Grüner, D.; Hansen, Th. C.; Rohrer, J.; Albe, K.; Fattakhova-Rohlfing, D.; Tietz, F. Phase-field determination of NaSICON materials in the quaternary system Na_2O-P_2O_5-SiO_2-ZrO_2: II. Glass-ceramics and the phantom of excessive vacancy formation. *Next Energy* **2024**, *4*, No. 100130.

(17) Oh, J. A. S.; He, L.; Plewa, A.; Morita, M.; Zhao, Y.; Sakamoto, T.; Song, X.; Zhai, W.; Zeng, K.; Lu, L. Composite NASICON ($Na_3Zr_2Si_2PO_{12}$) Solid-State Electrolyte with Enhanced Na^+ Ionic Conductivity: Effect of Liquid Phase Sintering. *ACS Appl. Mater. Interfaces* **2019**, *11*, 40125–40133.

(18) Wang, H.; Zhao, G.; Wang, S.; Liu, D.; Mei, Z.; An, Q.; Jiang, J.; Guo, H. Enhanced ionic conductivity of a $Na_3Zr_2Si_2PO_{12}$ solid electrolyte with Na_2SiO_3 obtained by liquid phase sintering for solid-state Na^+ batteries. *Nanoscale* **2022**, *14*, 823–832.

(19) Santhoshkumar, B.; Choudhary, M. B.; Bera, A. K.; Yusuf, S. M.; Ghosh, M.; Pahari, B. High Na^+ conducting $Na_3Zr_2Si_2PO_{12}$/$Na_2Si_2O_5$ composites as solid electrolytes for Na^+ batteries. *J. Am. Ceram. Soc.* **2022**, *105*, 5011–5019.

(20) Suzuki, K.; Noi, K.; Hayashi, A.; Tatsumisago, M. Low temperature sintering of $Na_{1+x}Zr_2Si_xP_{3-x}O_{12}$ by the addition of Na_3BO_3. *Scripta Mater.* **2018**, *145*, 67–70.

(21) Kutsuzawa, D.; Kobayashi, T.; Komiya, S. Flux-Assisted Low-Temperature Fabrication of Highly Durable All-Oxide Solid-State Sodium-Ion Batteries. *ACS Appl. Energy Mater.* **2022**, *5*, 4025–4028.

(22) Guo, H.; Baker, A.; Guo, J.; Randall, C. A. Cold Sintering Process: A Novel Technique for Low-Temperature Ceramic Processing of Ferroelectrics. *J. Am. Ceram. Soc.* **2016**, *99*, 3489–3507.

(23) Funahashi, S.; Guo, J.; Guo, H.; Wang, K.; Baker, A. L.; Shiratsuyu, K.; Randall, C. A. Demonstration of the Cold Sintering Process Study for the Densification and Grain Growth of ZnO Ceramics. *J. Am. Ceram. Soc.* **2017**, *100*, 546–553.

(24) Bang, S. H.; Ndayishimiye, A.; Randall, C. A. Anisothermal densification kinetics of the cold sintering process below 150 °C. *J. Mater. Chem. C* **2020**, *8*, 5668–5672.

(25) Guo, J.; Floyd, R.; Lowum, S.; Maria, J.-P.; Herisson de Beauvoir, Th.; Seo, J.-H.; Randall, C. A. Cold Sintering: Progress, Challenges, and Future Opportunities. *Annu. Rev. Mater. Res.* **2019**, *49*, 275–295.

(26) Grady, Z. M.; Tsuji, K.; Ndayishimiye, A.; Seo, J.-H.; Randall, C. A. Densification of a Solid-State NASICON Sodium-Ion Electrolyte Below 400°C by Cold Sintering with a Fused Hydroxide Solvent. *ACS Appl. Energy Mater.* **2020**, *3*, 4356–4366.

(27) Pereira da Silva, J. G.; Bram, M.; Laptev, A. M.; Gonzalez-Julian, J.; Ma, Q.; Tietz, F.; Guillon, O. Sintering of a sodium-based NASICON electrolyte: A comparative study between cold, field assisted and conventional sintering methods. *J. Eur. Ceram. Soc.* **2019**, *39*, 2697–2702.

(28) Leng, H.; Huang, J.; Nie, J.; Luo, J. Cold sintering and ionic conductivities of $Na_{3.256}Mg_{0.128}Zr_{1.872}Si_2PO_{12}$ solid electrolytes. *J. Power Sources* **2018**, *391*, 170–179.

(29) Leng, H.; Nie, J.; Luo, J. Combining cold sintering and Bi_2O_3-Activated liquid-phase sintering to fabricate high-conductivity Mg-doped NASICON at reduced temperatures. *J. Materiomics* **2019**, *5*, 237–246.

(30) Ma, Q.; Guin, M.; Naqash, S.; Tsai, C.-L.; Tietz, F.; Guillon, O. Scandium-Substituted $Na_3Zr_2(SiO_4)_2(PO_4)$ Prepared by a Solution-Assisted Solid-State Reaction Method as Sodium-Ion Conductors. *Chem. Mater.* **2016**, *28*, 4821–4828.

(31) Lowum, S.; Floyd, R.; Maria, J.-P. Hydroflux-assisted densification: applying flux crystal growth techniques to cold sintering. *J. Mater. Sci.* **2020**, *55*, 12747–12760.

(32) Degen, T.; Sadki, M.; Bron, E.; König, U.; Nénert, G. The high score suite. *Powder Diffract.* **2014**, *29*, S13–S18.

(33) Kraus, W.; Nolze, G. Powder Cell—a program for the representation and manipulation of crystal structures and calculation for the resulting X-ray powder patterns. *J. Appl. Crystallogr.* **1996**, *29*, 301–303.

(34) Park, H.; Jung, K.; Nezafati, M.; Kim, Ch.-S.; Kang, B. Sodium Ion Diffusion in Nasicon ($Na_3Zr_2Si_2PO_{12}$) Solid Electrolytes: Effects of Excess Sodium. *ACS Appl. Mater. Interfaces* **2016**, *8*, 27814–27824.

(35) Naqash, S.; Tietz, F.; Yazhenskikh, E.; Müller, M.; Guillon, O. Impact of sodium excess on electrical conductivity of $Na_3Zr_2Si_2PO_{12}$ + x Na_2O ceramics. *Solid State Ionics* **2019**, *336*, 57–66.

(36) Naqash, S.; Sebold, D.; Tietz, F.; Guillon, O. Microstructure-conductivity relationship of $Na_3Zr_2(SiO_4)_2(PO_4)$ ceramics. *J. Am. Ceram. Soc.* **2019**, *102*, 1057–1070.

(37) Liu, Y.; Sun, Q.; Wang, D.; Adair, K.; Liang, J.; Sun, X. Development of the cold sintering process and its application in solid-state lithium batteries. *J. Power Sources* **2018**, *393*, 193–203.

(38) Irvine, J. T. S.; Sinclair, D. C.; West, A. R. Electroceramics: Characterisation by ac Impedance Spectroscopy. *Adv. Mater.* **1990**, *2*, 132–138.

(39) Tietz, F.; Odenwald, Ph.; Sebold, D.; Schaller, M.; Böger, T.; Köttgen, J.; Ma, Q.; Indris, S.; Zeier, W. G.; Cojocaru-Miredin, O.; Fattakhova-Rohlfing, D. Impact of Microstructural Properties on Ionic and Heat Transport in NaSICON Glass-Ceramics. *Batteries & Supercaps* **2025**.